Wave-equation inversion of time-lapse seismic data sets

Gboyega Ayeni and Biondo Biondi

ABSTRACT

We propose a linearized wave-equation inversion formulation for time-lapse seismic data sets. Our method poses time-lapse imaging as a joint least-squares problem that utilizes target-oriented approximations to the Hessian of the objective function. Because our method accounts for illumination mismatches —caused by differences in acquisition geometries— and for band-limited wave-propagation effects, it provides better estimates of production-related changes in reservoir acoustic properties than conventional time-lapse processing methods. Using data sets from a North Sea field, we demonstrate how our method can be used to image differences between time-lapse data sets. Furthermore, we show that obstruction artifacts may be attenuated by wave-equation inversion.

INTRODUCTION

Reservoir rock and fluid property changes can be obtained from seismic amplitude and/or travel-time changes (Lumley, 1995; Calvert, 2005). Several successful applications of time-lapse seismic imaging to reservoir monitoring have been published by previous authors (Lefeuvre et al., 2003; Whitcombe et al., 2004; Ebaid et al., 2009).

However, in practice, production-related changes in time-lapse seismic images can be masked by non-repeatability artifacts (e.g., changes in geometry, ambient noise). To correctly interpret time-lapse seismic differences, such artifacts must be attenuated —a prerequisite conventionally achieved through image cross-equalization methods (Rickett and Lumley, 2001). Although cross-equalization methods are well developed and provide reliable results in many practical applications, they are inadequate where large inconsistencies exist between time-lapse data sets or where the reservoir overburden is complex. Where these conventional methods fail, wave-equation inversion provides a way to attenuate unwanted artifacts in time-lapse images, thereby enhancing production-related changes.

The proposed method is based on linear least-squares migration/inversion of seismic data sets (Nemeth et al., 1999; Kühl and Sacchi, 2003; Clapp, 2005). Because each iteration of a data space implementation of least-squares migration/inversion is approximately twice the migration cost, this approach is expensive. However, by posing this problem in the image space, it can be efficiently solved in a target-oriented way (Valenciano et al., 2006; Tang, 2008). For the time-lapse imaging problem, we

can either invert for the complete baseline and monitor images or we can invert for a static baseline and time-lapse images between surveys. The input vectors in the resulting formulations contain the migrated images (or combinations thereof) and the output vector contains the inverted images. The operators are a concatenations of target-oriented approximations to the Hessian of the least-squares objective function (Ayeni and Biondi, 2010). We regularize the inversion using spatial (dip) and temporal (difference) constraints.

Because we assume that the data contain only primaries, robust multiple/noise attenuation is required prior to inversion. Furthermore, we assume compaction and velocity changes between surveys are small, therefore these can be removed by warping of the monitor images to the baseline.

First, we discuss linearized wave-equation inversion of time-lapse data sets. Then, we apply this method to a North Sea field time-lapse data set. We show that even with the presence of a gap (caused by a simulated obstruction) in the monitor data-set, wave-equation inversion give improved results over conventional methods.

METHODOLOGY

Given a linearized modeling operator $\mathbf{L}$, the seismic data $\mathbf{d}$ for survey i due to a reflectivity model $\mathbf{m}$ is

$$\mathbf{d}_i = \mathbf{L}_i \mathbf{m}_i. \tag{1}$$

Assuming we have two data sets (baseline $\mathbf{d}_0$ and monitor $\mathbf{d}_1$) acquired at different times over an evolving reservoir, joint least-squares migration/inversion involves solving the regression

$$\left[\begin{array}{cc} \mathbf{L}_0 & \mathbf{0} \\ \mathbf{0} & \mathbf{L}_1 \\ \hline \epsilon_0\mathbf{R}_0 & \mathbf{0} \\ \mathbf{0} & \epsilon_1\mathbf{R}_1 \\ \hline -\zeta_0\Lambda_0 & \zeta_1\Lambda_1 \end{array}\right] \left[\begin{array}{c} \mathbf{m}_0 \\ \mathbf{m}_1 \end{array}\right] \approx \left[\begin{array}{c} \mathbf{d}_0 \\ \mathbf{d}_1 \\ \hline \mathbf{0} \\ \mathbf{0} \\ \hline \mathbf{0} \end{array}\right], \tag{2}$$

where $\mathbf{R}_i$ and Λ_i are the spatial and temporal regularization operators respectively, and ϵ_i and ζ_i are the corresponding regularization parameters. Although we can directly solve equation 2 by minimizing the quadratic-norm of the regression (Ajo-Franklin et al., 2005), we choose to transform it to an image space problem of the form (Appendix A)

$$\left[\begin{array}{cc} \mathbf{H_0} & \mathbf{0} \\ \mathbf{0} & \mathbf{H_1} \\ \hline \mathbf{R_{00}} & \mathbf{0} \\ \mathbf{0} & \mathbf{R_{11}} \\ \hline \Lambda_{00} & -\Lambda_{01} \\ -\Lambda_{10} & \Lambda_{11} \end{array}\right] \left[\begin{array}{c} \hat{\mathbf{m}}_0 \\ \hat{\mathbf{m}}_1 \end{array}\right] \approx \left[\begin{array}{c} \tilde{\mathbf{m}}_0 \\ \tilde{\mathbf{m}}_1 \\ \hline \mathbf{0} \\ \mathbf{0} \\ \hline \mathbf{0} \\ \mathbf{0} \end{array}\right], \tag{3}$$

where $\mathbf{H}_i = \mathbf{L}_i^T \mathbf{L}_i$ is the wave-equation Hessian, and $\mathbf{R}_{ii} = \epsilon_i^2 \mathbf{R}_i^T \mathbf{R}_i$ and $\Lambda_{ij} = \zeta_i \Lambda_i{}^T \zeta_j \Lambda_j$ are the spatial and temporal constraints. Note that $\mathbf{L}^T$, the migration operator, is the adjoint of the modeling operator $\mathbf{L}$. The inverted time-lapse image $\Delta\hat{\mathbf{m}}$ is then the difference between the inverted baseline and monitor images ($\hat{\mathbf{m}}_0$ and $\hat{\mathbf{m}}_1$). Alternatively, we can re-write equation 3 to invert directly for the time-lapse image and a static baseline image (Appendix A). Furthermore, equation 3 can be extended to multiple seismic data sets (Ayeni and Biondi, 2010).

As shown in Appendix A, if there are physical movements of reflectors and velocity changes (e.g., due to reservoir depletion and compaction) between surveys, the baseline and monitor images will not be aligned. Such misalignments must be accounted for before or during inversion. As is the case in many practical time-lapse monitoring problems, we assume that the monitor data are migrated with the baseline velocity. The updated inversion problem is then given by (Appendix A)

$$\left[\begin{array}{cc} \mathbf{H}_0 & \mathbf{0} \\ \mathbf{0} & \mathbf{H}_1^b \\ \hline \mathbf{R}_{00} & \mathbf{0} \\ \mathbf{0} & \mathbf{R}_{11}^b \\ \hline \mathbf{\Lambda}_{00} & -\mathbf{\Lambda}_{01}^b \\ -\mathbf{\Lambda}_{10}^b & \mathbf{\Lambda}_{11}^b \end{array}\right] \left[\begin{array}{c} \hat{\mathbf{m}}_0 \\ \hat{\mathbf{m}}_1^b \end{array}\right] \approx \left[\begin{array}{c} \tilde{\mathbf{m}}_0 \\ \tilde{\mathbf{m}}_1^b \\ \hline \mathbf{0} \\ \mathbf{0} \\ \hline \mathbf{0} \\ \mathbf{0} \end{array}\right], \tag{4}$$

where $\tilde{\mathbf{m}}_1^b$ and $\hat{\mathbf{m}}_1^b$ are respectively the migrated and inverted monitor images repositioned (warped) to the baseline image. The superscript ^{b} on the operators denotes that they are referenced to the baseline image. For example, $\mathbf{H}_1^b$ is the Hessian matrix with the monitor geometry but with the baseline velocity. Note that whereas the conventional time-lapse image $\Delta\tilde{\mathbf{m}}^b$ estimated at the baseline position is given by

$$\Delta\tilde{\mathbf{m}}^b = \tilde{\mathbf{m}}_1^b - \tilde{\mathbf{m}}_0, \tag{5}$$

the inverted time-lapse image $\Delta\hat{\mathbf{m}}^b$ is given by

$$\Delta\hat{\mathbf{m}}^b = \hat{\mathbf{m}}_1^b - \hat{\mathbf{m}}_0. \tag{6}$$

The wave-equation Hessian at image point $\mathbf{x}$ is defined as (Plessix and Mulder, 2004; Valenciano et al., 2006)

$$H(\mathbf{x}, \mathbf{x}') = \sum_{\omega} \omega^4 \sum_{\mathbf{x}_s} |f_s(\omega)|^2 G(\mathbf{x}_s, \mathbf{x}, \omega) \bar{G}(\mathbf{x}_s, \mathbf{x}', \omega) \sum_{\mathbf{x}_r} G(\mathbf{x}, \mathbf{x}_r, \omega) \bar{G}(\mathbf{x}', \mathbf{x}_r, \omega), \tag{7}$$

where $\mathbf{x}'$ denotes all image points, $\bar{G}$ is the complex conjugate of Green's function G at frequency ω, f_s is the source function, and $\mathbf{x}_s$ and $\mathbf{x}_r$ are the source and receiver

positions, respectively. For any practical application, it is infeasible (and unnecessary) to compute the full Hessian matrix. Because the problem is posed in the image space, we only need to compute the Hessian for a target region of interest around the reservoir. In addition, we only compute off-diagonal elements sufficient to capture the dominant structure of the Hessian. This target-oriented approximation of the Hessian is given by (Valenciano et al., 2006)

$$H\left(\mathbf{x_T}, \mathbf{x_{T+a_x}}\right) = \sum_{\omega} \omega^4 \sum_{\mathbf{x_s}} |f\left(s\right)|^2 G(\mathbf{x_s}, \mathbf{x_T}, \omega) \bar{G}(\mathbf{x_s}, \mathbf{x_{T+a_x}}, \omega) \sum_{\mathbf{x_r}} G(\mathbf{x_T}, \mathbf{x_r}, \omega) \bar{G}(\mathbf{x_{T+a_x}}, \mathbf{x_r}, \omega), \tag{8}$$

where $\mathbf{x_T}$ is an image point within the target area, and $\mathbf{x_{T+a_x}}$ represents points within a *small* region around $\mathbf{x_T}$. For any image point, elements of $\mathbf{H}\left(\mathbf{x_T}, \mathbf{x_{T+a_x}}\right)$ represents a row of a sparse Hessian matrix $\mathbf{H}$ whose non-zero components are defined by $\mathbf{a_x}$. Therefore, $\mathbf{a_x}$ defines the how many off-diagonal elements of the Hessian are computed — which represents the size of the point spread function (PSF) around each image point. Note that because of symmetry, only one half of the approximate Hessian is required. The target-oriented Hessian and computational savings are discussed in further detail by Valenciano et al. (2006) and Tang (2008).

In this paper, the spatial regularization operators are non-stationary dip filters. First, we estimate the local dips on the migrated baseline image using a plane-wave destruction method (Fomel, 2002). Then we construct the operator based on factorization of directional Laplacian representations of the local dip filters (Hale, 2007). The temporal constraint is implemented as a difference between the aligned images. To attenuate multiples and other unwanted artifacts in the data, we perform a high-resolution Radon demultiple on the data. In order to align the baseline and monitor images prior to inversion, we perform pre-stack warping using a cyclic local cross-correlation method (Ayeni, 2010).

In the next section, we apply the proposed method to a field time-lapse data set. We show applications to complete and incomplete monitor data sets.

EXAMPLE

We apply the proposed method to a North Sea time-lapse data set with two years of production between the baseline and the monitor. The shots and receivers are spaced at 25 m, and the maximum offset is 3200 m. First, we show how wave-equation inversion can improve time-lapse amplitude information on complete data sets. In this example, the baseline and monitor data sets have similar geometries. Secondly, we simulate an obstruction in the monitor data with a gap 400 m wide. In this example, except at the obstruction where no sources or receivers are present in the monitor, the baseline and monitor data sets have similar geometries. Figure 1 shows the full migrated baseline stacked section. After preliminary processing of the

data, we identified the reservoir location around which the target area for inversion is defined. Henceforth, we show the results only for the target area. All inversion results are obtained using the RJMI formulation.

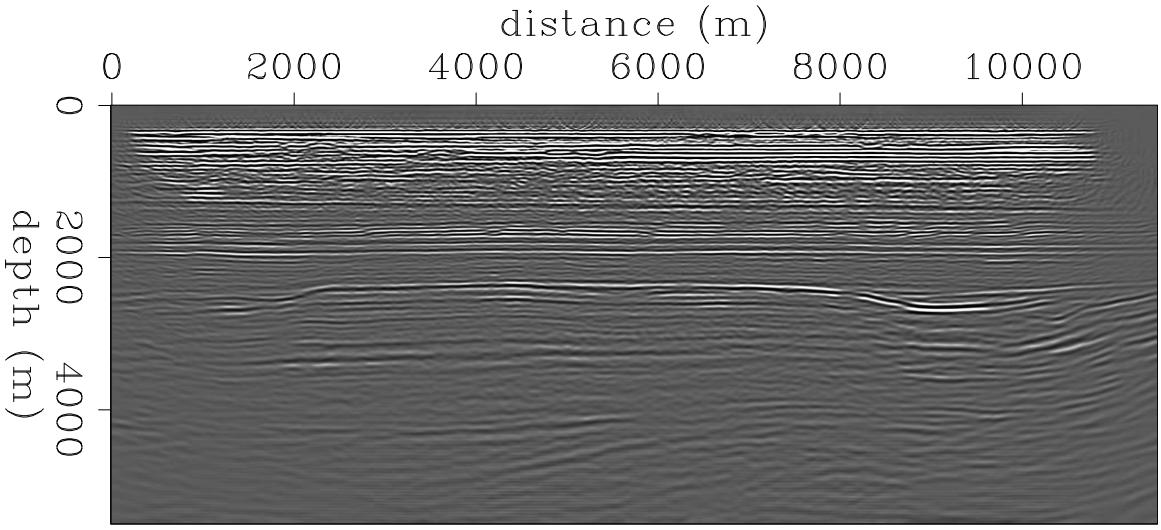

Figure 1: Raw baseline stacked image. [**CR**]

Example 1: Complete baseline and monitor data

Figure 2 shows the migrated pre-stack image obtained from the raw baseline data set. Note in Figure 2 that multiples show significant curvature relative to the correctly-migrated flat primaries. The same image after multiple attenuation is shown in Figure 3. In order to remove small velocities errors, we applied a residual moveout correction to the image gathers. The pre-processed pre-stack monitor image is shown in Figure 4. To obtain this image, in addition to the pre-processing applied to the baseline, we also applied a bulk amplitude correction to the monitor data. We estimate the amplitude correction as the ratio between the root-mean-square energy in the baseline versus the monitor. In addition, we perform pre-stack warping of the monitor to the baseline image. Apparent vertical displacements between the baseline and monitor are shown in Figure 5. Figure 6 shows the Hessian diagonal for the target area. Local dip estimates obtained from the stacked baseline image (not shown) are shown in Figure 7. Figure 8 shows the time-lapse images after different processing steps. Note the incremental improvements in the time-lapse image quality after processing and after inversion.

Example 2: Complete baseline and Incomplete monitor data

Figure 9 shows that gapped monitor data. Here, we simulate an obstruction in the geometry such that neither sources nor receivers are present between 2500 and 2900

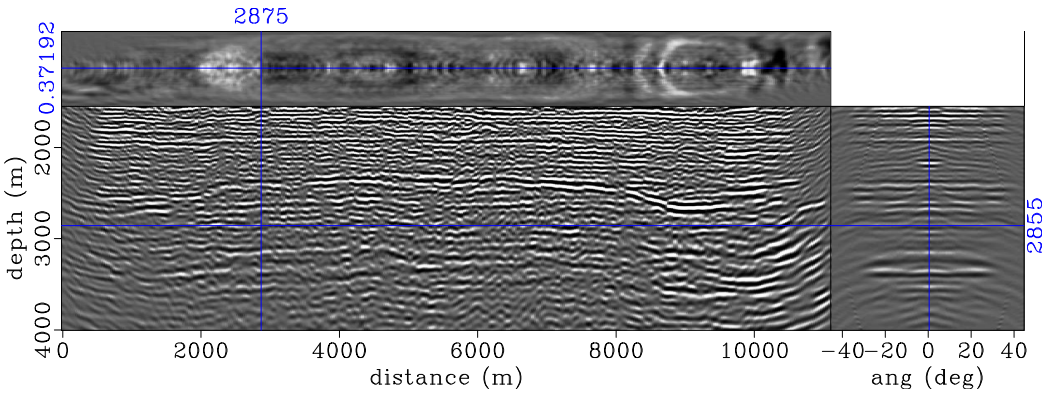

Figure 2: Raw pre-stack baseline image for the target area. Note the presence of several multiples and other undesired artifacts. [**CR**]

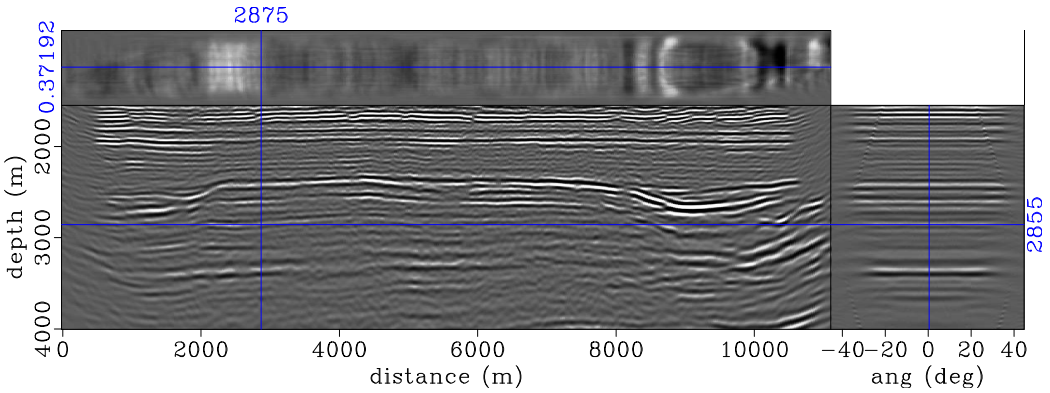

Figure 3: Preprocessed pre-stack baseline image of the target area. Note that the artifacts in the raw image (Figure 2) have been attenuated. [**CR**]

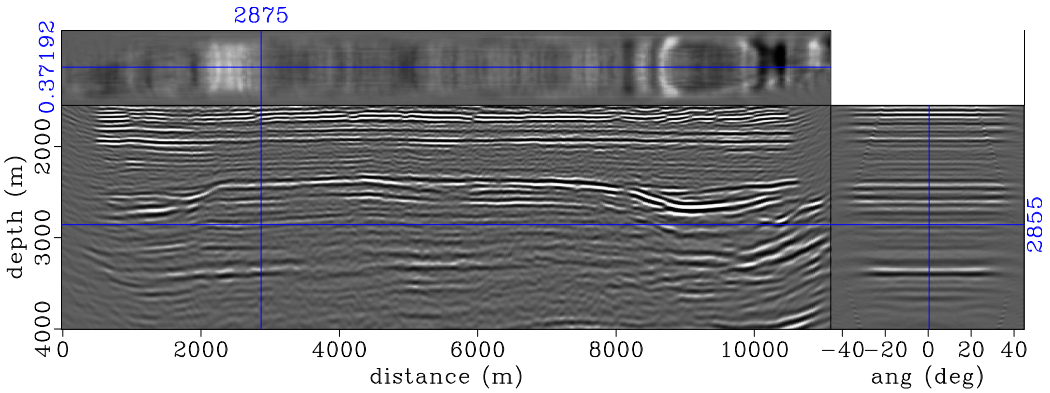

Figure 4: Preprocessed pre-stack monitor image of the target area obtained using the same parameters as in the baseline (Figure 3). Note that this image has been warped (using apparent displacements in Figures 5) to the baseline image. [**CR**]

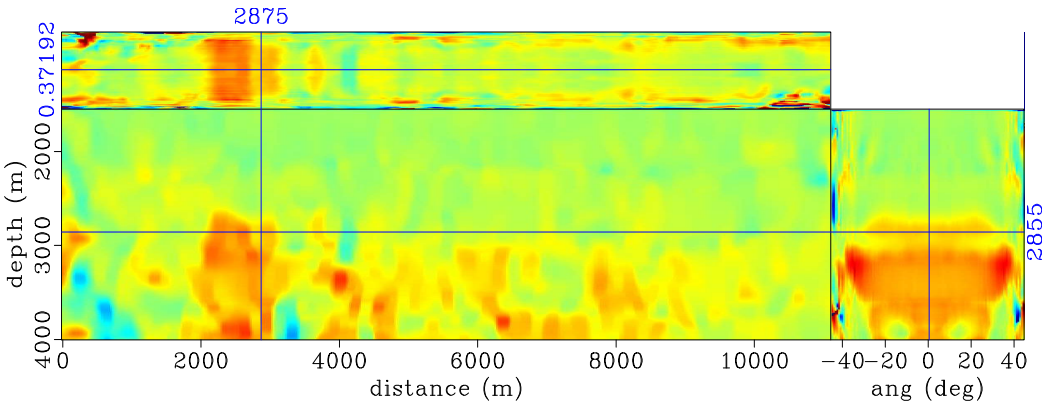

Figure 5: Apparent vertical displacements between the baseline and monitor images (Figures 3 and 4). Red, blue and green denote positive, negative and zero displacements respectively. Note that the maximum apparent displacements correspond to the reservoir location between position 2000 m to 3000 m. Also, note that the apparent displacement varies with opening angle. [**CR**]

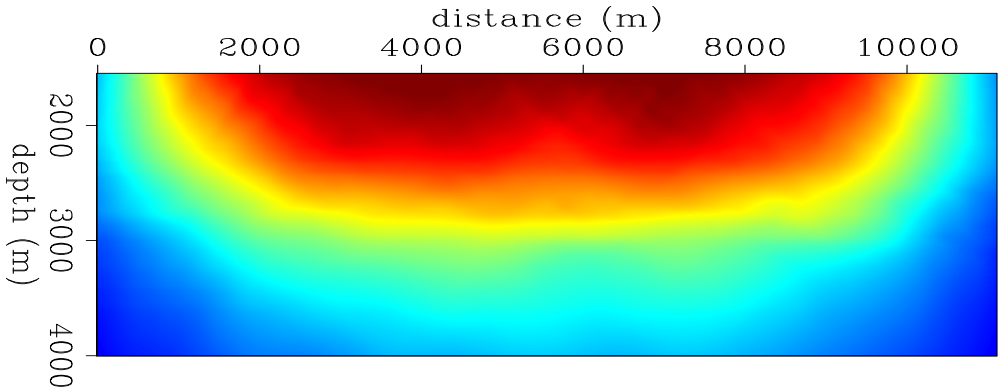

Figure 6: Illumination (Hessian diagonal) for the target area. Red indicates high illumination whereas blue indicates low illumination. [**CR**]

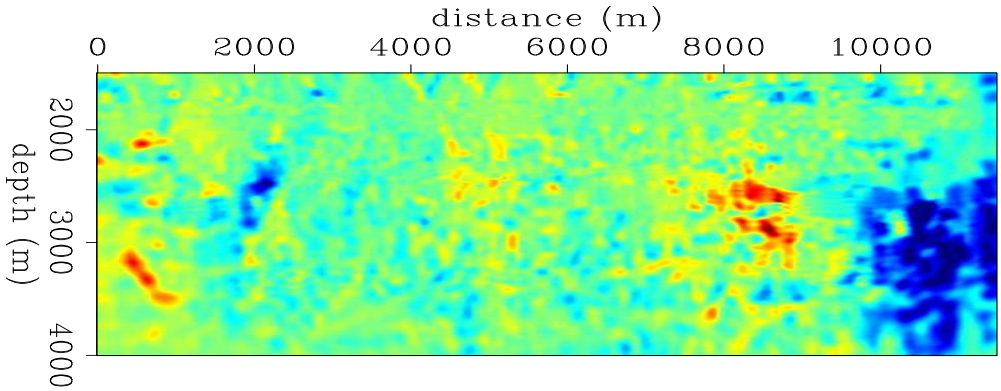

Figure 7: Dip estimates obtained from the stacked baseline image. Red indicates positive dips whereas blue indicates negative dips. These dip estimates are used to construct the spatial regularization operator. [**CR**]

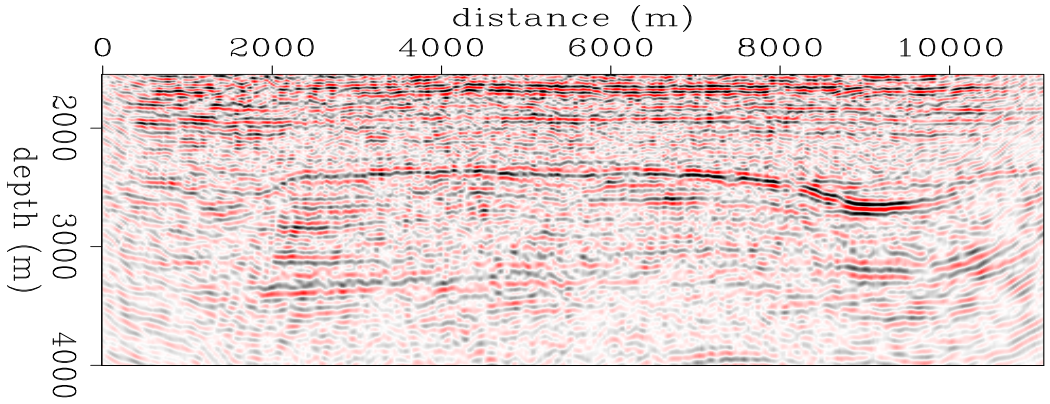

(a)

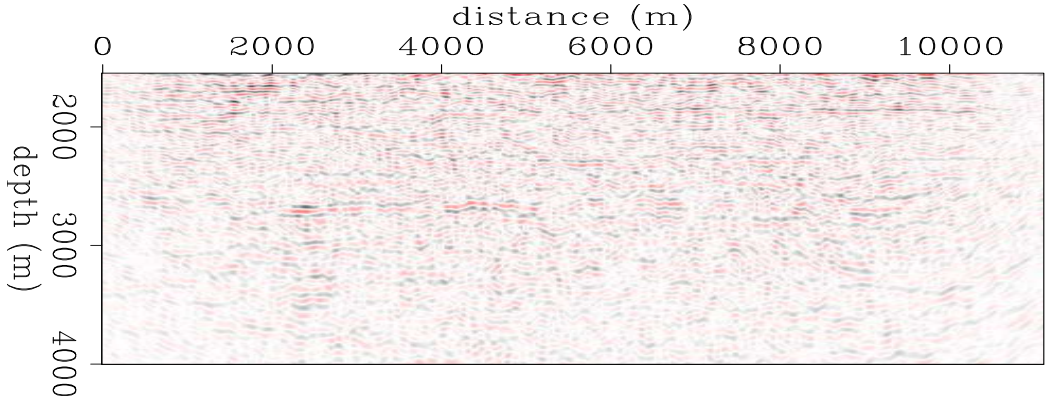

(b)

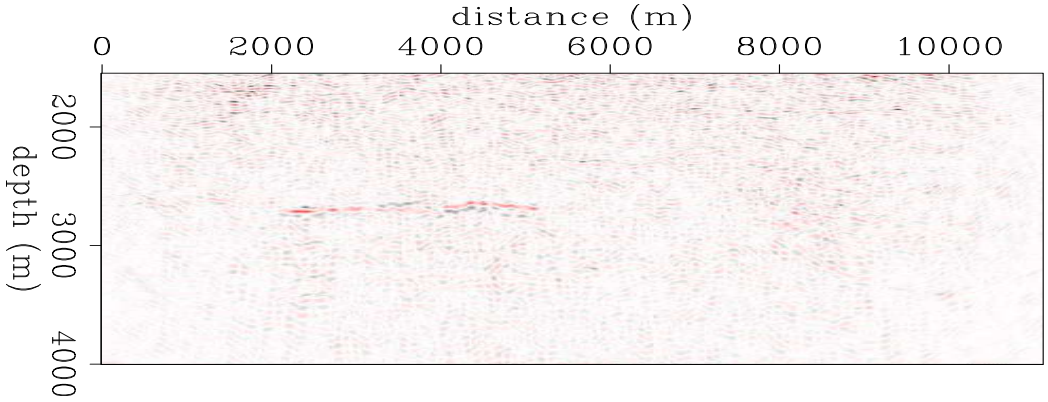

(c)

Figure 8: Time-lapse images (a) from the raw data, (b) after time-lapse processing and (c) after wave-equation inversion. Note the incremental improvements in the time-lapse image from (a) to (c). [**CR**]

m. This gap in the the data coincides with the reservoir location. We image gapped monitor data using the same parameters and in the previous example. However, in order to warp this incomplete monitor to the complete baseline, we first perform Radon interpolation to fill in the monitor gap. The interpolated monitor data are then imaged and processed using the same parameters as in the complete monitor case. The resulting pre-stack image is then used to estimate the apparent displacement vectors (Figure 10) used to warp the incomplete monitor image to the baseline. The ratio of the Hessian diagonal (illumination ratio) between the baseline and monitor is shown Figure 11. Note that the region with low illumination ratios correspond to the location of the simulated obstruction. Figures 12 and 13 show the spatial and wavenumber domain point-spread-functions (PSFs) at point $x = 2600$ m and $z = 2600$ m, respectively. Note that there is significant differences in the PSFs away from the diagonal (center of the spatial PSF) and at various wavenumbers. Figure 14 shows the time-lapse images after different processing steps. Note the incremental improvements in the time-lapse image quality after processing and after inversion. Furthermore, note that compared to the complete data example (Figure 8(b)), the time-lapse image from conventional processing (Figure 14(b)) is of poorer quality.

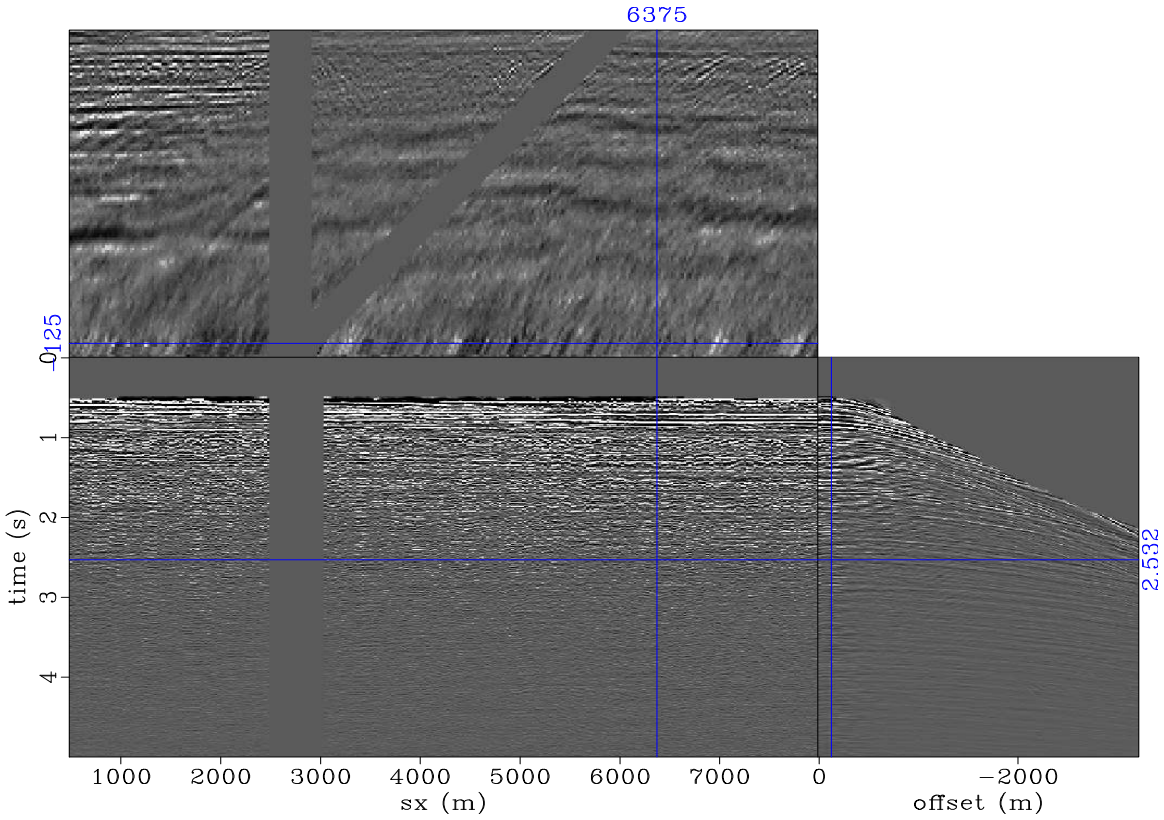

Figure 9: Gapped monitor data. Note that we have sources and receivers are missing around within the simulated obstruction. [**CR**]

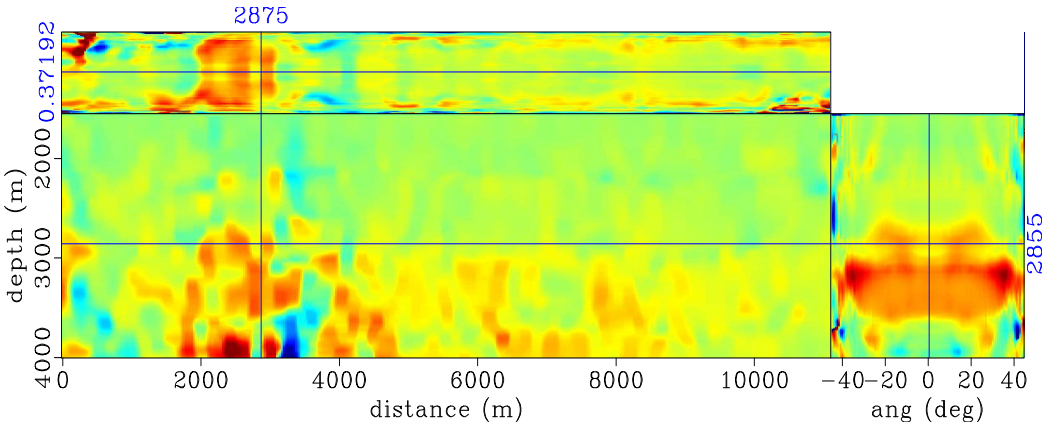

Figure 10: Apparent vertical displacements between images from the baseline and interpolated monitor data sets. Comparing this to Figure 5, note that estimates of the apparent displacements are similar to those from the complete data case. [**CR**]

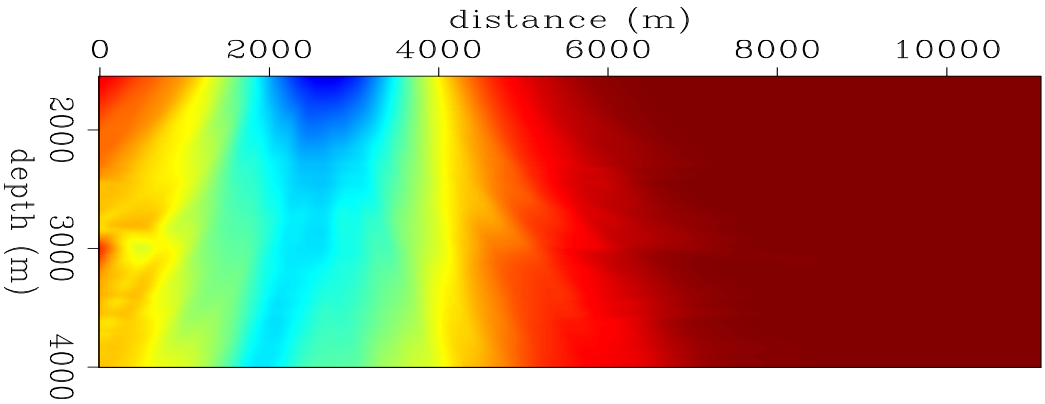

Figure 11: Illumination ratio between the baseline and monitor. Red indicates regions with equal illumination (i.e., ratio equals unity) whereas blue indicates unequal illumination (i.e., ratio less than unity). [**CR**]

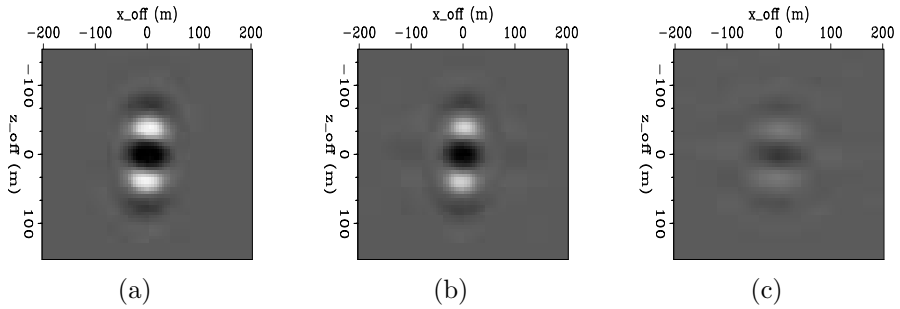

Figure 12: Point-spread-functions at point $x = 2600$ m and $z = 2600$ m for the (a) baseline and (b) monitor. Note in the difference PSF (c), that there is significant energy away from the center of the PSF (i.e. in the off-diagonal parts of the Hessian). [**CR**]

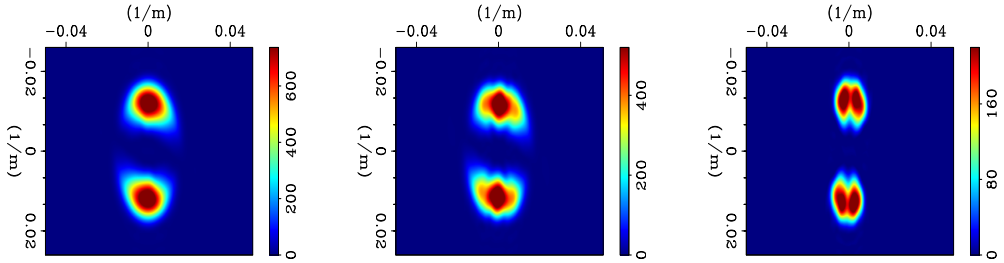

(a) (b) (c)

Figure 13: Wavenumber domain point-spread-functions at point $x = 2600$ m and $z = 2600$ m for the (a) baseline and (b) monitor. Note in the difference PSF (c), that there is significant illumination differences at various wavenumbers. [**CR**]

DISCUSSION

Data preprocessing sufficiently attenuates multiples and other artifacts in the data (Figures 2 and 3). This is required to ensure that the data satisfy sufficiently the primaries-only assumption in our inversion formulation. By warping the images before stacking, we ensure that defocusing effects due to velocity and compaction effects are minimized. Because the overburden geology along the studied section is fairly simple, the monitor image (Figure 4) is sufficiently aligned to the baseline using only vertical components of the prestack apparent displacement vectors (Figure 5). In practice, even with good repeatability between surveys, it is difficult to interpret an unprocessed time-lapse image (Figure 8(a)). However, after careful processing, it is possible to make meaningful interpretation of amplitude information in the time-lapse image (Figure8(b)). Although in many cases, results from a conventional processing workflow may suffice, the quality of the time-lapse image can be improved by wave-equation inversion (Figure 8(c)). In the second example, because the monitor data is incomplete, the effective geometries differ for the two surveys, thereby leading to illumination mismatch (i.e., illumination ratios not equal to unity) in parts of the target area (Figure 11). However, the Hessian diagonal gives only a partial measure of the illumination mismatch between time-lapse surveys (Figure 11). Large geometry differences (e.g., an obstruction in the monitor acquisition) can cause large differences in the off-diagonal terms of the Hessian (Figure 12). Such geometry differences lead to differences in wavenumber illumination between surveys (Figure 13). Therefore, a point-by-point amplitude compensation using only the Hessian diagonal is inadequate. Where there is significant geometry difference between surveys, conventional time-lapse processing is insufficient (Figure 14(b)). In this case, wave-equation inversion provides a significant improvement to the time-lapse image (Figure 14(c)). Although the amplitude information derivable from the interpolated monitor data (not shown) are of poor quality the kinematics are similar to those of the complete baseline image. Therefore these provide adequate estimates of the warping parameters (Figure 10) comparable to those from the complete data case (Figure 5).

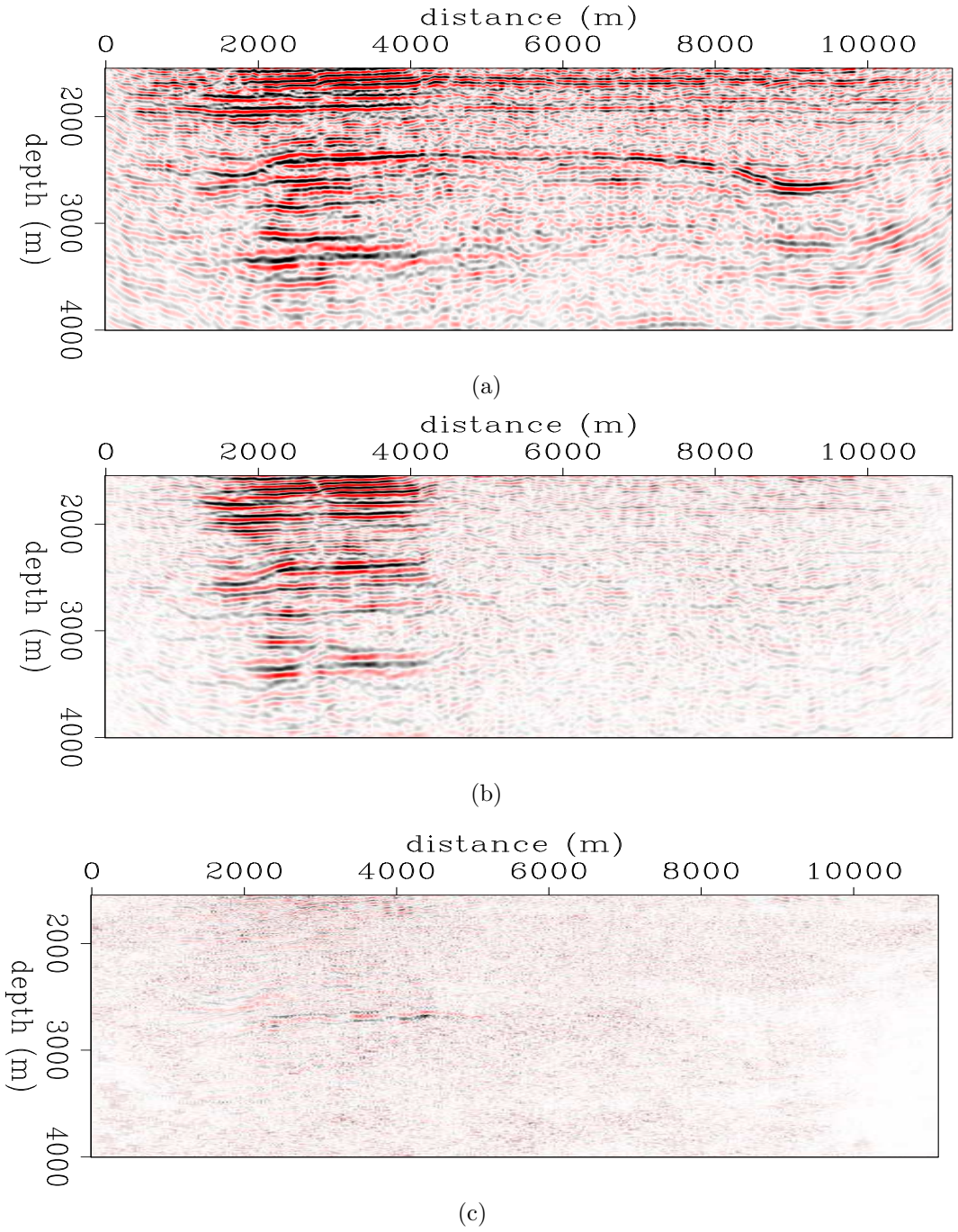

Figure 14: Time-lapse images (a) from the raw data, (b) after time-lapse processing and (c) after wave-equation inversion. Also, because of artifacts introduced by the incomplete monitor data, conventional methods fail to provide results of comparable quality to the complete data example (Figure 8(b)). Note that inversion provides satisfactory results. [**CR**]

CONCLUSIONS

We have proposed a wave-equation inversion scheme for time-lapse seismic data sets. Applying the proposed method to a North sea field data set shows that it can improve production-related time-lapse seismic responses. This method can improve time-lapse amplitude information and can be used to attenuate artifacts caused by geometry/illumination differences between surveys.

ACKNOWLEDGMENTS

We thank Statoil and partners (ENI and Petoro) for donating the field data set used in this study. We thank the Stanford Center for Computational Earth & Environmental Science (CEES) for providing the computer resources used in this study.

APPENDIX A

Assuming we have two data sets (baseline $\mathbf{d}_0$ and monitor $\mathbf{d}_1$) acquired at different times, the following sections shows derivations of the the joint inversion formulations for image differences and for multiple images.

Joint Inversion for Image Differences (JID)

We can formulate baseline and monitor data modeling as follows:

$$\begin{bmatrix} \mathbf{L}_0 & \mathbf{0} \\ \mathbf{L}_1 & \mathbf{L}_1 \end{bmatrix} \begin{bmatrix} \mathbf{m}_0 \\ \mathbf{\Delta m} \end{bmatrix} = \begin{bmatrix} \mathbf{d}_0 \\ \mathbf{d}_1 \end{bmatrix}, \tag{A-1}$$

which can be divided into the following two parts:

$$\mathbf{L}_0\mathbf{m}_0 = \mathbf{d}_0, \tag{A-2}$$

$$\mathbf{L}_1\mathbf{m}_0 + \mathbf{L}_1\mathbf{\Delta m} = \mathbf{d}_1, \tag{A-3}$$

where the time-lapse reflectivity image $\mathbf{\Delta m}$ is given by

$$\mathbf{\Delta m} = \mathbf{m}_1 - \mathbf{m}_0. \tag{A-4}$$

Note that Equation A-1 assumes that both $\mathbf{m}_0$ and $\mathbf{m}_1$ are collocated. This means that there is no physical movement of the reflector between the baseline and the monitor images. In addition, equation A-1 assumes that there are no overburden velocity changes. If stress changes cause any physical movement of a point from baseline position (x_0, y_0, z_0) in $\mathbf{m}_0$ to monitor position (x_1, y_1, z_1) in $\mathbf{m}_1$, we can update

equation A-3 such that the point in $\mathbf{m}_0$ is repositioned at (x_1, y_1, z_1). The updated modeling equation for the monitor data then becomes

$$\mathbf{L}_1\mathbf{S}^{m-}\mathbf{m}_0 + (\mathbf{L}_1\mathbf{m}_1 - \mathbf{L}_1\mathbf{S}^{m-}\mathbf{m}_0) = \mathbf{L}_1\mathbf{S}^{m-}\mathbf{m}_0 + \mathbf{L}_1\mathbf{\Delta m}^m = \mathbf{d}_1, \tag{A-5}$$

where $\mathbf{S}^{m-}$ is an orthogonal warping operator that aligns $\mathbf{m}_0$ to $\mathbf{m}_1$, and

$$\mathbf{\Delta m}^m = \mathbf{m}_1 - \mathbf{S}^{m-}\mathbf{m}_0 \tag{A-6}$$

is the time-lapse image estimated at the monitor position (x_1, y_1, z_1). And the combined modeling equation becomes

$$\begin{bmatrix} \mathbf{L}_0 & \mathbf{0} \\ \mathbf{L}_1\mathbf{S}^{m-} & \mathbf{L}_1 \end{bmatrix} \begin{bmatrix} \mathbf{m}_0 \\ \mathbf{\Delta m}^m \end{bmatrix} \approx \begin{bmatrix} \mathbf{d}_0 \\ \mathbf{d}_1 \end{bmatrix}. \tag{A-7}$$

However, note that equation A-7 requires that we know the true reflector position in the monitor which we may obtain from a geomechanical model. Furthermore, any regularization on the time-lapse image must be applied at the monitor position, or by first repositioning the time-lapse image to the baseline position as follows:

$$\mathbf{\Delta m} = \mathbf{\Delta m}^b = \mathbf{S}^{m+}\mathbf{\Delta m}^m, \tag{A-8}$$

where $\mathbf{\Delta m}^b$ is the time-lapse image at the baseline position and $\mathbf{S}^{m+} = (\mathbf{S}^{m-})^{-1}$ is an operator that repositions events from the monitor position to the baseline position.

Assuming we migrate the monitor data with the true monitor velocity, we arrive at the image-space inversion problem by minimizing the quadratic-norm

$$\left\| \begin{bmatrix} \mathbf{L}_0 & \mathbf{0} \\ \mathbf{L}_1\mathbf{S}^{m-} & \mathbf{L}_1 \end{bmatrix} \begin{bmatrix} \mathbf{m}_0 \\ \mathbf{\Delta m}^m \end{bmatrix} - \begin{bmatrix} \mathbf{d}_0 \\ \mathbf{d}_1 \end{bmatrix} \right\| \approx 0 \tag{A-9}$$

for which the solutions $\hat{\mathbf{m}}_0$ and $\hat{\mathbf{\Delta m}}^m$ satisfy the solution

$$\begin{bmatrix} \mathbf{L}_0^T\mathbf{L}_0 + \mathbf{S}^{m+}\mathbf{L}_1^T\mathbf{L}_1\mathbf{S}^{m-} & \mathbf{S}^{m+}\mathbf{L}_1^T\mathbf{L}_1 \\ \mathbf{L}_1^T\mathbf{L}_1\mathbf{S}^{m-} & \mathbf{L}_1^T\mathbf{L}_1 \end{bmatrix} \begin{bmatrix} \hat{\mathbf{m}}_0 \\ \hat{\mathbf{\Delta m}}^m \end{bmatrix} \approx \begin{bmatrix} \mathbf{L}_0^T & \mathbf{S}^{m+}\mathbf{L}_1^T \\ \mathbf{0} & \mathbf{L}_1^T \end{bmatrix} \begin{bmatrix} \mathbf{d}_0 \\ \mathbf{d}_1 \end{bmatrix}, \tag{A-10}$$

or simply

$$\begin{bmatrix} \mathbf{H}_0 + \mathbf{S}^{m+}\mathbf{H}_1\mathbf{S}^{m-} & \mathbf{S}^{m+}\mathbf{H}_1 \\ \mathbf{H}_1\mathbf{S}^{m-} & \mathbf{H}_1 \end{bmatrix} \begin{bmatrix} \hat{\mathbf{m}}_0 \\ \hat{\mathbf{\Delta m}}^m \end{bmatrix} \approx \begin{bmatrix} \tilde{\mathbf{m}}_0 + \mathbf{S}^{m+}\tilde{\mathbf{m}}_1 \\ \tilde{\mathbf{m}}_1 \end{bmatrix}. \tag{A-11}$$

Note that the time-lapse image we obtain is $\hat{\mathbf{\Delta m}}^m$ at the monitor position and not $\hat{\mathbf{\Delta m}} = \hat{\mathbf{\Delta m}}^b$ at the baseline position. Although what is most interesting is $\hat{\mathbf{\Delta m}}^m$, as shown later in this section, we may choose to re-write the formulation as a function of $\hat{\mathbf{\Delta m}}^b$.

Assuming we migrate the monitor data with the wrong (e.g. baseline) velocity, then equation A-10 becomes

$$\begin{bmatrix} \mathbf{L}_0^T\mathbf{L}_0 + \mathbf{S}^{\alpha+}\check{\mathbf{L}}_1^T\mathbf{L}_1\mathbf{S}^{m-} & \mathbf{S}^{m+}\check{\mathbf{L}}_1^T\mathbf{L}_1 \\ \check{\mathbf{L}}_1^T\mathbf{L}_1\mathbf{S}^{m-} & \check{\mathbf{L}}_1^T\mathbf{L}_1 \end{bmatrix} \begin{bmatrix} \hat{\mathbf{m}}_0 \\ \hat{\mathbf{\Delta m}}^m \end{bmatrix} \approx \begin{bmatrix} \mathbf{L}_0^T & \mathbf{S}^{\alpha+}\check{\mathbf{L}}_1^T \\ \mathbf{0} & \check{\mathbf{L}}_1^T \end{bmatrix} \begin{bmatrix} \mathbf{d}_0 \\ \mathbf{d}_1 \end{bmatrix}, \tag{A-12}$$

where $\check{\mathbf{L}}_1^T$, the migration operator with the monitor geometry but with baseline velocity migrates the monitor data to apparent position (x_1', y_1', z_1'), and $\mathbf{S}^{\alpha+}$ repositions the migrated data from (x_1', y_1', z_1') to (x_0, y_0, z_0). However, because the operator $\mathbf{L}_1$ is a function of the true monitor velocity, if the true monitor velocity is known, we should solve equation A-11 instead of equation A-12. Note that in the case where the monitor migration velocity is the correct one, equation A-12 becomes equation A-11. If we have neither the true monitor velocity nor a geomechanical model, we may modify the Hessian in equation A-12 using the apparent displacements between (x_1', y_1', z_1') and (x_0, y_0, z_0) so we can approximate equation A-12 as

$$\begin{bmatrix} \mathbf{L}_0^T\mathbf{L}_0 + \mathbf{S}^{\alpha+}\check{\mathbf{L}}_1^T\check{\mathbf{L}}_1\mathbf{S}^{\alpha-} & \mathbf{S}^{\alpha+}\check{\mathbf{L}}_1^T\check{\mathbf{L}}_1 \\ \check{\mathbf{L}}_1^T\check{\mathbf{L}}_1\mathbf{S}^{\alpha-} & \check{\mathbf{L}}_1^T\check{\mathbf{L}}_1 \end{bmatrix} \begin{bmatrix} \hat{\mathbf{m}}_0 \\ \boldsymbol{\Delta}\hat{\mathbf{m}}^a \end{bmatrix} \approx \begin{bmatrix} \mathbf{L}_0^T & \mathbf{S}^{\alpha+}\check{\mathbf{L}}_1^T \\ \mathbf{0} & \check{\mathbf{L}}_1^T \end{bmatrix} \begin{bmatrix} \mathbf{d}_0 \\ \mathbf{d}_1 \end{bmatrix}, \quad \text{(A-13)}$$

Then equation A-11 becomes

$$\begin{bmatrix} \mathbf{H}_0 + \mathbf{S}^{\alpha+}\check{\mathbf{H}}_1\mathbf{S}^{\alpha-} & \mathbf{S}^{\alpha+}\check{\mathbf{H}}_1 \\ \check{\mathbf{H}}_1\mathbf{S}^{\alpha-} & \check{\mathbf{H}}_1 \end{bmatrix} \begin{bmatrix} \hat{\mathbf{m}}_0 \\ \boldsymbol{\Delta}\hat{\mathbf{m}}^a \end{bmatrix} \approx \begin{bmatrix} \tilde{\mathbf{m}}_0 + \mathbf{S}^{\alpha+}\tilde{\mathbf{m}}_1 \\ \tilde{\mathbf{m}}_1^a \end{bmatrix}, \quad \text{(A-14)}$$

where $\check{\mathbf{H}}_1$ is the modified Hessian in which we account for the mis-positioning due to compaction and velocity change. To account for such mis-positioning, we compute the updated Hessian using perturbed Green's functions:

$$\begin{aligned} \check{H}\left(\mathbf{y_T}, \mathbf{y_{T+a_x}}\right) = \sum_{\omega} \omega^4 \sum_{\mathbf{y_s}} |f\left(s\right)|^2 G_\alpha(\mathbf{y_s}, \mathbf{y_T}, \omega)\bar{G}_\alpha(\mathbf{y_s}, \mathbf{y_{T+a_y}}, \omega) \\ \sum_{\mathbf{y_r}} G_\alpha(\mathbf{y_T}, \mathbf{y_r}, \omega)\bar{G}_\alpha(\mathbf{y_{T+a_y}}, \mathbf{y_r}, \omega), \end{aligned} \quad \text{(A-15)}$$

where $\mathbf{y}$ denotes an apparent point in the monitor image that corresponds to baseline point $\mathbf{x}$. The modified Green's function G_α is given by

$$G_\alpha = G(\mathbf{x}) \exp^{-i\omega\Delta t_\alpha} \approx G(\mathbf{x}) \exp^{-i\omega\frac{|\mathbf{x}_\alpha|}{v_o}}, \quad \text{(A-16)}$$

where Δt_α is the time-delay corresponding to the absolute apparent displacement $|\mathbf{x}_\alpha|$ and v_o is the baseline velocity.

Instead of inverting for the time-lapse image at the monitor position, another approach is to directly invert for $\boldsymbol{\Delta}\hat{\mathbf{m}}^b = \boldsymbol{\Delta}\hat{\mathbf{m}}$ at the baseline position by making the substitution

$$\boldsymbol{\Delta}\mathbf{m}^m = \mathbf{S}^{m-}\boldsymbol{\Delta}\mathbf{m} \quad \text{(A-17)}$$

into equation A-9 to obtain

$$\begin{bmatrix} \mathbf{L}_0 & \mathbf{0} \\ \mathbf{L}_1\mathbf{S}^{m-} & \mathbf{L}_1\mathbf{S}^{m-} \end{bmatrix} \begin{bmatrix} \mathbf{m}_0 \\ \boldsymbol{\Delta}\mathbf{m} \end{bmatrix} \approx \begin{bmatrix} \mathbf{d}_0 \\ \mathbf{d}_1 \end{bmatrix} \quad \text{(A-18)}$$

which leads to the image-space problem

$$\begin{bmatrix} \mathbf{H}_0 + \mathbf{S}^{m+}\mathbf{H}_1\mathbf{S}^{m-} & \mathbf{S}^{m+}\mathbf{H}_1\mathbf{S}^{m-} \\ \mathbf{S}^{m+}\mathbf{H}_1\mathbf{S}^{m-} & \mathbf{S}^{m+}\mathbf{H}_1\mathbf{S}^{m-} \end{bmatrix} \begin{bmatrix} \hat{\mathbf{m}}_0 \\ \boldsymbol{\Delta}\hat{\mathbf{m}} \end{bmatrix} \approx \begin{bmatrix} \tilde{\mathbf{m}}_0 + \mathbf{S}^{m+}\tilde{\mathbf{m}}_1 \\ \mathbf{S}^{m+}\tilde{\mathbf{m}}_1 \end{bmatrix} = \begin{bmatrix} \tilde{\mathbf{m}}_0 + \tilde{\mathbf{m}}_1^b \\ \tilde{\mathbf{m}}_1^b \end{bmatrix}. \quad \text{(A-19)}$$

where $\tilde{\mathbf{m}}_1^b$, the migrated monitor image repositioned to the baseline position (x_0, y_0, z_0), is defined as

$$\tilde{\mathbf{m}}_1^b = \mathbf{S}^{m+}\tilde{\mathbf{m}}_1. \tag{A-20}$$

If we migrate the monitor data with the baseline velocity, equation A-19 becomes

$$\begin{bmatrix} \mathbf{H}_0 + \mathbf{S}^{\alpha+}\check{\mathbf{H}}_1\mathbf{S}^{\alpha-} & \mathbf{S}^{\alpha+}\check{\mathbf{H}}_1\mathbf{S}^{\alpha-} \\ \mathbf{S}^{\alpha+}\check{\mathbf{H}}_1\mathbf{S}^{\alpha-} & \mathbf{S}^{\alpha+}\check{\mathbf{H}}_1\mathbf{S}^{\alpha-} \end{bmatrix} \begin{bmatrix} \hat{\mathbf{m}}_0 \\ \boldsymbol{\Delta}\hat{\mathbf{m}} \end{bmatrix} \approx \begin{bmatrix} \tilde{\mathbf{m}}_0 + \mathbf{S}^{\alpha+}\tilde{\mathbf{m}}_1^a \\ \mathbf{S}^{\alpha+}\tilde{\mathbf{m}}_1^a \end{bmatrix} = \begin{bmatrix} \tilde{\mathbf{m}}_0 + \tilde{\mathbf{m}}_1^b \\ \tilde{\mathbf{m}}_1^b \end{bmatrix}, \tag{A-21}$$

where,

$$\mathbf{S}^{\alpha+}\tilde{\mathbf{m}}_1^a \approx \tilde{\mathbf{m}}_1^b = \mathbf{S}^{m+}\tilde{\mathbf{m}}_1. \tag{A-22}$$

However, provided the velocity change is isotropic, compaction effects are small, differences in kinematics are small, and the velocity change is small, we can make the following approximation:

$$\mathbf{L}_1\mathbf{S}^{m-}\mathbf{m}_1^b \approx \mathbf{U}^{m-}\mathbf{L}_1^b\mathbf{m}_1^b = \mathbf{d}_1, \tag{A-23}$$

where the operator $\mathbf{L}_1$ is a function of both the monitor velocity and geometry, whereas $\mathbf{L}_1^b$ is a function of the baseline velocity but the monitor geometry. $\mathbf{U}^{m-}$ is an orthogonal operator that translates a data due to a reflectivity spike at baseline position (x_0, y_0, z_0) and baseline background velocity v_0, to data due to a spike at (x_1, y_1, z_1) and monitor background velocity v_1. Note that in equation A-23, we have made the following approximation

$$\mathbf{U}^{m-} \approx \mathbf{L}_1\mathbf{S}^{m-}\left[\left[(\mathbf{L}_1^b)^T\mathbf{L}_1^b\right]^{-1}(\mathbf{L}_1^b)^T\right]. \tag{A-24}$$

Provided equation A-23 holds, we can write

$$(\mathbf{L}_1^b)^T(\mathbf{U}^{m-})^T\mathbf{U}^{m-}\mathbf{L}_1^b\mathbf{m}_1^b \approx (\mathbf{L}_1^b)^T(\mathbf{U}^{m-})^T\mathbf{d}_1, \tag{A-25}$$

where,

$$\begin{gathered}(\mathbf{U}^{m-})^T\mathbf{U}^{m-} = (\mathbf{U}^{m-})^{-1}\mathbf{U}^{m-} = \mathbf{U}^{m+}\mathbf{U}^{m-} = \mathbf{I}, \\ (\mathbf{L}_1^b)^T(\mathbf{U}^{m-})^T = \mathbf{S}^{m+}\mathbf{L}_1^T.\end{gathered} \tag{A-26}$$

Therefore, we can write

$$(\mathbf{L}_1^b)^T\mathbf{L}_1^b\mathbf{m}_1^b \approx \mathbf{S}^{m+}\mathbf{L}_1^T\mathbf{L}_1\mathbf{S}^{m-}\mathbf{m}_1^b \approx \mathbf{S}^{m+}\mathbf{L}_1^T\mathbf{d}_1 \approx \tilde{\mathbf{m}}_1^b, \tag{A-27}$$

where, $(\mathbf{L}_1^b)^T\mathbf{L}_1^b = \mathbf{H}_1^b$ is the Hessian computed using the baseline velocity but with the monitor geometry. Making these substitutions into equation A-19, we have

$$\begin{bmatrix} \mathbf{H}_0 + \mathbf{H}_1^b & \mathbf{H}_1^b \\ \mathbf{H}_1^b & \mathbf{H}_1^b \end{bmatrix} \begin{bmatrix} \hat{\mathbf{m}}_0 \\ \boldsymbol{\Delta}\hat{\mathbf{m}} \end{bmatrix} \approx \begin{bmatrix} \tilde{\mathbf{m}}_0 + \tilde{\mathbf{m}}_1^b \\ \tilde{\mathbf{m}}_1^b \end{bmatrix}. \tag{A-28}$$

An important advantage of the formulation in equation A-28 is that it allows us to readily regularize the time-lapse image. However, it may be desirable to invert directly for the individual seismic images, as shown in the following sections.

Joint Inversion of Multiple Images (JMI)

We can pose the problem as an inversion for the individual (baseline and monitor) images. Then, the modeling equation becomes

$$\begin{bmatrix} \mathbf{L}_0 & \mathbf{0} \\ \mathbf{0} & \mathbf{L}_1 \end{bmatrix} \begin{bmatrix} \mathbf{m}_0 \\ \mathbf{m}_1 \end{bmatrix} = \begin{bmatrix} \mathbf{d}_0 \\ \mathbf{d}_1 \end{bmatrix} . \tag{A-29}$$

Using the same assumptions and procedure as in the previous section, we arrive at the following formulation:

$$\begin{bmatrix} \mathbf{H}_0 & \mathbf{0} \\ \mathbf{0} & \mathbf{H}_1 \end{bmatrix} \begin{bmatrix} \hat{\mathbf{m}}_0 \\ \hat{\mathbf{m}}_1 \end{bmatrix} \approx \begin{bmatrix} \tilde{\mathbf{m}}_0 \\ \tilde{\mathbf{m}}_1 \end{bmatrix} , \tag{A-30}$$

where the baseline and monitor velocities are known. Where the monitor has been aligned with baseline, we have

$$\begin{bmatrix} \mathbf{H}_0 & \mathbf{0} \\ \mathbf{0} & \mathbf{H}_1^b \end{bmatrix} \begin{bmatrix} \hat{\mathbf{m}}_0 \\ \hat{\mathbf{m}}_1^b \end{bmatrix} \approx \begin{bmatrix} \tilde{\mathbf{m}}_0 \\ \tilde{\mathbf{m}}_1^b \end{bmatrix} , \tag{A-31}$$

which holds approximately whether or not we migrate the monitor data with the baseline or monitor velocity.

Regularized Joint inversion of Multiple Images (RJMI)

Because in the JMI formulation, the models are completely decoupled, they can be regularized by minimizing the norm

$$\left\| \begin{bmatrix} \epsilon_0\mathbf{R}_0 & \mathbf{0} \\ \mathbf{0} & \epsilon_1\mathbf{R}_1 \end{bmatrix} \begin{bmatrix} \hat{\mathbf{m}}_0 \\ \hat{\mathbf{m}}_1 \end{bmatrix} \right\| \approx 0 , \tag{A-32}$$

where $\mathbf{R}_i$ is the spatial regularization operator and ϵ_i the spatial regularization parameter for survey i. To add any temporal regularization, we need to warp the inverted monitor images to the baseline and then apply temporal constraints or we can regularize the time-lapse image directly by minimizing the norm:

$$\left\| \begin{bmatrix} -\zeta_0\mathbf{\Lambda_0} & \zeta_1\mathbf{\Lambda}_1 \end{bmatrix} \begin{bmatrix} \hat{\mathbf{m}}_0 \\ \hat{\mathbf{m}}_1 \end{bmatrix} \right\| \approx 0 , \tag{A-33}$$

where Λ_i is the temporal regularization operator and ζ_i is the regularization parameter. Therefore the full regularized inversion requires a minimization of the norm:

$$\left\| \begin{bmatrix} \mathbf{L}_0 & \mathbf{0} \\ \mathbf{0} & \mathbf{L}_1 \\ \hline \epsilon_0\mathbf{R}_0 & \mathbf{0} \\ \mathbf{0} & \epsilon_1\mathbf{R}_1 \\ \hline -\zeta_0\mathbf{\Lambda}_0 & \zeta_1\mathbf{\Lambda}_1 \end{bmatrix} \begin{bmatrix} \hat{\mathbf{m}}_0 \\ \hat{\mathbf{m}}_1 \end{bmatrix} - \begin{bmatrix} \mathbf{d}_0 \\ \mathbf{d}_1 \\ \hline \mathbf{0} \\ \mathbf{0} \\ \hline \mathbf{0} \end{bmatrix} \right\| \approx 0 , \tag{A-34}$$

which leads to the image-space problem

$$\left[\begin{array}{cc} \mathbf{H}_0 & \mathbf{0} \\ \mathbf{0} & \mathbf{H}_1 \\ \hline \mathbf{R}_{00} & \mathbf{0} \\ \mathbf{0} & \mathbf{R}_{11} \\ \hline \mathbf{\Lambda}_{00} & -\mathbf{\Lambda}_{01} \\ -\mathbf{\Lambda}_{10} & \mathbf{\Lambda}_{11} \end{array}\right] \left[\begin{array}{c} \hat{\mathbf{m}}_0 \\ \hat{\mathbf{m}}_1 \end{array}\right] \approx \left[\begin{array}{c} \tilde{\mathbf{m}}_0 \\ \tilde{\mathbf{m}}_1 \\ \hline \mathbf{0} \\ \mathbf{0} \\ \hline \mathbf{0} \\ \mathbf{0} \end{array}\right], \tag{A-35}$$

where $\mathbf{R}_{ii} = \epsilon_i^2 \mathbf{R}_i^T \mathbf{R}_i$ and $\mathbf{\Lambda}_{ij} = \zeta_i \mathbf{\Lambda}_i^T \zeta_j \mathbf{\Lambda}_j$ are the spatial and temporal constraints, respectively.

If the monitor has been aligned to the baseline, then we can impose the spatial regularization by minimizing

$$\left\| \left[\begin{array}{cc} \epsilon_0 \mathbf{R}_0 & \mathbf{0} \\ \mathbf{0} & \epsilon_1 \mathbf{R}_1^b \end{array}\right] \left[\begin{array}{c} \hat{\mathbf{m}}_0 \\ \hat{\mathbf{m}}_1^b \end{array}\right] \right\| \approx 0 \ , \tag{A-36}$$

and the temporal regularization by minimizing

$$\left\| \left[\begin{array}{cc} -\zeta_0 \mathbf{\Lambda_0} & \zeta_1 \mathbf{\Lambda}_1^b \end{array}\right] \left[\begin{array}{c} \hat{\mathbf{m}}_0 \\ \hat{\mathbf{m}}_1^b \end{array}\right] \right\| \approx 0 \ , \tag{A-37}$$

where $\mathbf{R}_1^b$ and $\mathbf{\Lambda}_1^b$ are defined with respect to the baseline-aligned monitor image. If the time-lapse image at the baseline position, the regularized image-space inversion problem is given by

$$\left[\begin{array}{cc} \mathbf{H}_0 & \mathbf{0} \\ \mathbf{0} & \mathbf{H}_1^b \\ \hline \mathbf{R}_{00} & \mathbf{0} \\ \mathbf{0} & \mathbf{R}_{11}^b \\ \hline \mathbf{\Lambda}_{00} & -\mathbf{\Lambda}_{01}^b \\ -\mathbf{\Lambda}_{10}^b & \mathbf{\Lambda}_{11}^b \end{array}\right] \left[\begin{array}{c} \hat{\mathbf{m}}_0 \\ \hat{\mathbf{m}}_1^b \end{array}\right] \approx \left[\begin{array}{c} \tilde{\mathbf{m}}_0 \\ \tilde{\mathbf{m}}_1^b \\ \hline \mathbf{0} \\ \mathbf{0} \\ \hline \mathbf{0} \\ \mathbf{0} \end{array}\right], \tag{A-38}$$

where the superscript $(^b)$ denotes that the operators and images are referenced to the baseline position. Note that in the simplest case, where the temporal regularization is a difference operator equation A-33 becomes

$$\left\| \zeta \left[\begin{array}{cc} -\mathbf{I} & \mathbf{S}^{m+} \end{array}\right] \left[\begin{array}{c} \hat{\mathbf{m}}_0 \\ \hat{\mathbf{m}}_1 \end{array}\right] \right\| \approx 0 \ , \tag{A-39}$$

and for the baseline-aligned images, the temporal constraint in equation A-37 becomes

$$\left\| \zeta \left[\begin{array}{cc} -\mathbf{I} & \mathbf{I} \end{array}\right] \left[\begin{array}{c} \hat{\mathbf{m}}_0 \\ \hat{\mathbf{m}}_1^b \end{array}\right] \right\| \approx 0 \ . \tag{A-40}$$

REFERENCES

Ajo-Franklin, J. B., J. Urban, and J. M. Harris, 2005, Temporal integration of seismic traveltime tomography: SEG Technical Program Expanded Abstracts, **24**, 2468–2471.

Ayeni, G., 2010, Cyclic 1d matching of time-lapse seismic data sets: A case study of the norne field: SEP Report, **140**.

Ayeni, G., and B. Biondi, 2010, Target-oriented joint least-squares migration/inversion of time-lapse seismic data sets: Geophysics, **75**, R61–R73.

Calvert, R., 2005, Insights and methods for 4D reservoir monitoring and characterization: SEG/EAGE DISC (Distinguished Instructor Lecture Course).

Clapp, M. L., 2005, Imaging under salt: illumination compensation by regularized inversion: PhD thesis, Stanford University.

Ebaid, H., M. Nasser, P. Hatchell, and D. Stanley, 2009, Time-lapse seismic makes a significant business impact at Holstein: SEG, Expanded Abstracts, **28**, 3810–3814.

Fomel, S., 2002, Applications of plane-wave destruction filters: Geophysics, **67**, 1946–1960.

Hale, D., 2007, Local dip filtering with directional Laplacians: CWP Project Reiew, **567**, 91–102.

Kühl, H., and M. D. Sacchi, 2003, Least-squares wave-equation migration for avp/ava inversion: Geophysics, **68**, 262–273.

Lefeuvre, F., Y. Kerdraon, J. Peliganga, S. Medina, P. Charrier, R. L'Houtellier, and D. Dubucq, 2003, Improved reservoir understanding through rapid and effective 4D: Girassol field, Angola, West Africa: SEG Technical Program Expanded Abstracts, **22**, 1334–1337.

Lumley, D. E., 1995, Seismic time-lapse monitoring of subsurface fluid flow: PhD thesis, Stanford University, http://sepwww.stanford.edu/public/docs/sep91/.

Nemeth, T., C. Wu, and G. T. Schuster, 1999, Least-squares migration of incomplete reflection data: Geophysics, **64**, 208–221.

Plessix, R.-E., and W. Mulder, 2004, Frequency-domain finite-frequency amplitude-preserving migration: Geophysical Journal International, **157**, 975–985.

Rickett, J. E., and D. E. Lumley, 2001, Cross-equalization data processing for time-lapse seismic reservoir monitoring: A case study from the Gulf of Mexico: Geophysics, **66**, 1015–1025.

Tang, Y., 2008, Wave-equation Hessian by phase encoding: SEG Technical Program Expanded Abstracts, **27**, 2201–2205.

Valenciano, A. A., B. Biondi, and A. Guitton, 2006, Target-oriented wave-equation inversion: Geophysics, **71**, A35–A38.

Whitcombe, D. N., J. M. Marsh, P. J. Clifford, M. Dyce, C. J. S. McKenzie, S. Campbell, A. J. Hill, R. S. Parr, C. Pearse, T. A. Ricketts, C. P. Slater, and O. L. Barkved, 2004, The systematic application of 4D in BP's North-West Europe operations — 5 years on: SEG Technical Program Expanded Abstracts, **23**, 2251–2254.